Open Access

Journal of Energy and Power Technology

LIDSEN Publishing Inc.

Original Research

Development of Wind IPMSG Based Bipolar DC Microgrids

Xiang-Yu Sun, Ping-Hong Jhou, Min-Ze Lu, Chang-Ming Liaw *

National Tsing Hua University, No. 101, Sec. 2, Guangfu Rd., East Dist., Hsinchu City, Taiwan (R.O.C.); E-Mails: sunxy95@gmail.com; zxc2130433@gmail.com; b10112016@gmail.com; cmliaw@ee.nthu.edu.tw

* **Correspondence:** Chang-Ming Liaw; E-Mail: cmliaw@ee.nthu.edu.tw

Academic Editor: Andrés Elías Feijóo Lorenzo

Collection: Wind Energy

Journal of Energy and Power Technology
2020, volume 3, issue 2
doi:10.21926/jept.2102028

Received: February 24, 2021
Accepted: May 28, 2021
Published: June 25, 2021

Abstract

This paper presents the development of a wind Interior Permanent-Magnet Synchronous Generator (IPMSG) based bipolar DC microgrids along with various switch-mode rectifiers. Firstly, the wind IPMSG is established and adequately controlled to possess satisfactory generating characteristics during different driven speeds and loads. Later, the boost switch-mode rectifier (SMR) based bipolar DC bus is established. Further, three-phase single-switch (3P1SW) boost SMR, three-phase two-switch (3P2SW) three-level boost SMR, and a three-phase three-switch (3P3SW) Vienna SMR are comparatively evaluated. Along with the proposed robust voltage and current controls, a well-regulated microgrid DC-bus voltage is established. Moreover, the voltage balancing control is proposed to minimize the imbalance in the bipolar DC-bus voltage. For the wind IPMSG having Vienna SMR, the commutation angle setting is adjusted to use the reluctance power component effectively.

Keywords

Microgrid; wind generator; IPMSG; bipolar DC bus; 3P1SW SMR; 3P2SW SMR; Vienna SMR; voltage balancing; control.

1. Introduction

Microgrids with renewable sources can be operated independently to reduce fossil energy consumption effectively [1-5]. Microgrids are classified into AC microgrid, DC microgrid, and AC/DC hybrid microgrid. Comparatively speaking, the DC microgrid has a few merits, such as a longer bus length, simpler and fewer interface converters used for sources and loads, etc. In constructing a DC microgrid, one can adopt a unipolar or bipolar bus structure. Compared with the former, bipolar shows higher reliability because of an open line fault, fewer power switches used to form load converters, etc.

Any electric machine can be operated as a generator and applied to construct a wind generator [6]. However, due to volumetric and weight limitations, AC machines are still the mainstream actuators. Compared with other machines, the permanent-magnet synchronous machine (PMSM) has the advantages of a simple structure, brushless without excitation-winding, high power density, etc. [7-10]. Owing to high-performance permanent magnet-material manufacturing technology improvement, wind power generation systems tend to use PMSG, especially the interior PMSG (IPMSG), for its rigid rotor and higher efficiency [11-13].

The AC/DC converter is an essential front-end for an electronic power plant powered by the utility grid. To have a better quality of line-drawn power and a well-regulated DC output voltage, one can adopt a suited SMR having power factor correction (PFC) control. The surveys for the existing SMRs can be found elsewhere [14-16]. A three-phase SMR has to be equipped as its following converter for a wind generator using three-phase AC machines. Normally, the boost type SMR is adopted to establish the common DC-bus voltage of the microgrid. Considering the schematic and the control, the possible SMRs for the wind generator may include: (i) three-phase single-switch (3P1SW) DCM SMR [17]; (ii) 3P1SW CCM SMR [14, 15]; (iii) three-phase two-switch (3P2SW) SMR [18]; (vi) three-phase three-switch (3P3SW) Vienna SMR [19, 20]; and (v) three-phase six-switch (3P6SW) full-bridge SMR. Since only unidirectional power capability is required for a wind generator, the Vienna SMR is considered to be the best schematic in making compromised considerations in switch number, the sinusoidal input current waveform PWM switching ability, and the switching losses. More importantly, the bipolar DC bus with three-level voltage switching can be formed naturally.

To integrate various harvested sources, energy storage devices, loads, and utility grids with the DC microgrid system, the proper power electronic converters based on their specific characteristics need to be employed. The AC/DC converter is used for the AC wind generator. The survey of the commonly used SMRs has been presented above. The function of the DC/DC converter is to adapt the input/output voltage levels. The DC/DC converters can be broadly classified into (i) isolation and non-isolation; (ii) single-port and multi-port; (iii) step-up, step-down and step-up/down; (iv) unidirectional and bidirectional; and (v) hard switching and soft switching [21-29]. While the unidirectional converters are applied for photovoltaic and solid-state fuel cells, the energy storage devices must adopt the bidirectional ones for achieving charging/discharging operations [24-29]. As for the local load and utility grid, they need to be interfaced with the DC microgrid common DC-bus via PWM inverters [30-34].

This paper presents a wind IPMSG-based bipolar DC microgrid followed by different SMRs. Compared to other topologies, the Vienna SMR offers acceptable performance regarding power quality, control flexibility, and unidirectional power flow. Furthermore, it is indicated that the

commutation instant shift should be properly adjusted to extract more power from the IPMSG, which can be considered for implementation in future wind IPMSG systems. Apart from the introduction section, the organization of this paper is listed as followed: (i) Section 2 presents the system configuration and problem statements. After providing the topologies and control schemes of the adopted SMRs, the used machines for the prime mover and the wind generator are introduced; (ii) The non-sinusoidal SMR based bipolar DC microgrid is provided in Section 3. It is found that the inherently large inductance of the IPMSG does not allow the SMR to operate normally under the DCM; hence two SMR topologies are used for evaluating comparatively; (iii) Section 4 introduces the three-phase Vienna SMR based bipolar DC microgrid. Through the proposed control schemes, it possesses a better line drawn power quality with a higher utilization rating. The commutation instant shift for the IPMSG with followed Vienna SMR can also be applied to increase the energy conversion efficiency; and finally, (iv) Section 5 provides the conclusion for this paper.

2. System Configurations and Problem Statements

2.1 The Studied Plants

Figure 1 shows the conceptual block diagram of a wind IPMSG based bipolar DC microgrid. A three-phase AC/DC converter is used as the following converter for the AC wind generator. A suitable type of SMR can be adopted to have good AC input and DC output characteristics. Further, the bipolar DC bus having well-regulated voltages is established using suitable schematics. The power stages being interfaced to the microgrid common DC bus may include battery energy storage system, local loads, utility grid, and other parts.

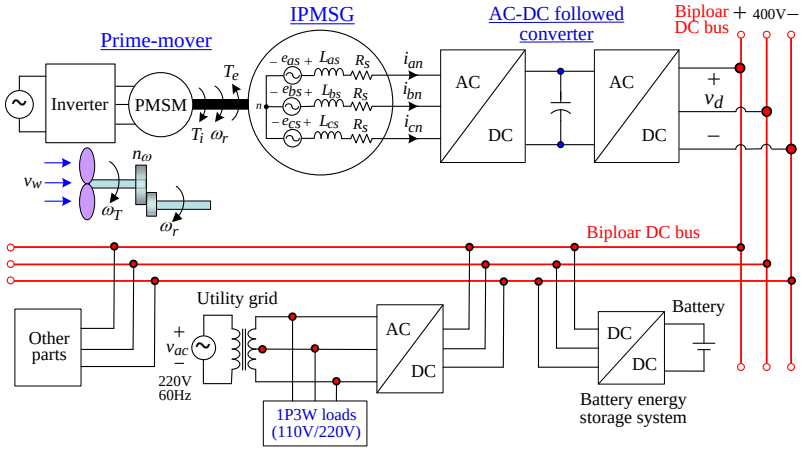

Figure 1 Conceptual block diagram of a wind IPMSG based bipolar DC microgrid.

The unidirectional SMR can be employed for a wind IPMSG. The simplest schematic of a wind IPMSG with 3P1SW DCM SMR for establishing the microgrid bipolar DC bus is depicted in Figure 2(a). The AC side energy storage inductors must be small enough to ensure the DCM operation for the overall load range [17]. The PFC function is then inherently preserved without applying current control. Figure 2(b) shows the voltage-mode direct duty control scheme. The bipolar DC-bus is established using a passive capacitor leg. If the inherent voltage imbalance needs to be avoided, one can use the IGBT voltage balancer as an alternative to replacing the capacitor leg.

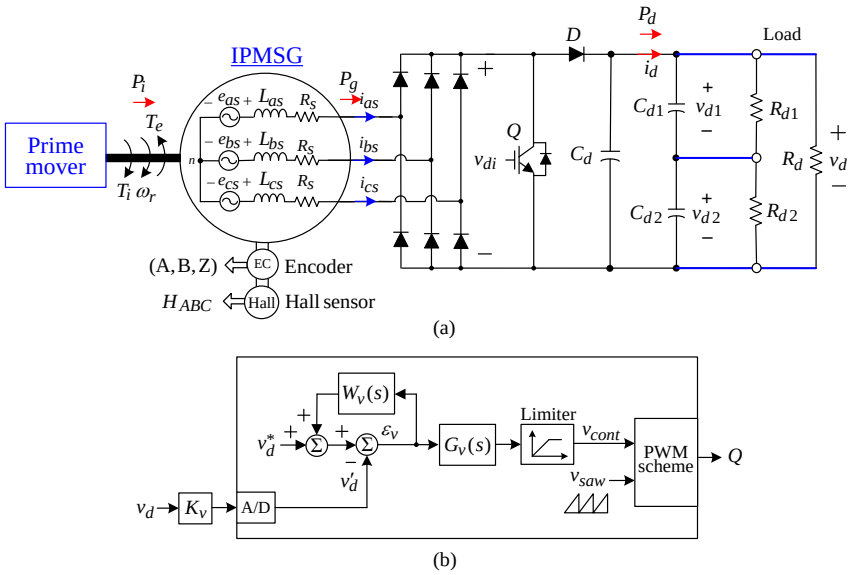

Figure 2 Wind IPMSG based bipolar DC microgrid with 3P1SW DCM boost SMR: (a) schematic; (b) control scheme.

For a utility grid-powered 3P1SW DCM SMR, the energy storage inductors are added externally, and they have certain limitations. However, analytic and experimental studies indicate that the limitation for low inductance of the energy storage inductor generally cannot be satisfied for the inherent PMSG armature winding inductance. The quantitative analyses will be presented later in Sec. 3.1.2.

To avoid the limitations of the energy storage inductor possessed by the 3P1SW DCM SMR, one can adopt the 3P1SW CCM SMR depicted in Figure 3(a). It is formed by inserting a CCM DC/DC boost converter between the diode rectifier and the capacitive filter. The standard cascade control scheme consisting of outer-voltage and inner-current loops is shown in Figure 3(b). Similarly, the bipolar DC bus is also formed by a capacitor leg. The voltage transfer relationship under various driving speeds of the developed wind IPMSG is depicted in Figure 3(c).

The wind IPMSG with 3P2SW CCM SMR and its control scheme are shown in Figures 4(a) and 4(b), wherein the proposed voltage balancing scheme is also arranged. The three-level bipolar DC-bus is inherently established.

Although the topologies of Figure 2 to Figure 4 are simple, they possess non-sinusoidal armature winding current with a low power factor and thus attain a low generator rating utilization. To solve this problem, one can adopt the three-phase three-switch (3P3SW) three-level Vienna rectifier depicted in Figure 5(a). Owing to its 3P3SW structure, the three-phase Vienna SMR can control three-phase currents separately to have a sinusoidal line drawn current having high rating utilization. Moreover, one can obtain higher power generating capacity for the IPMSG by adjusting the commutation shift angle. The control scheme of the wind IPMSG with Vienna SMR is shown in Figure 5(b).

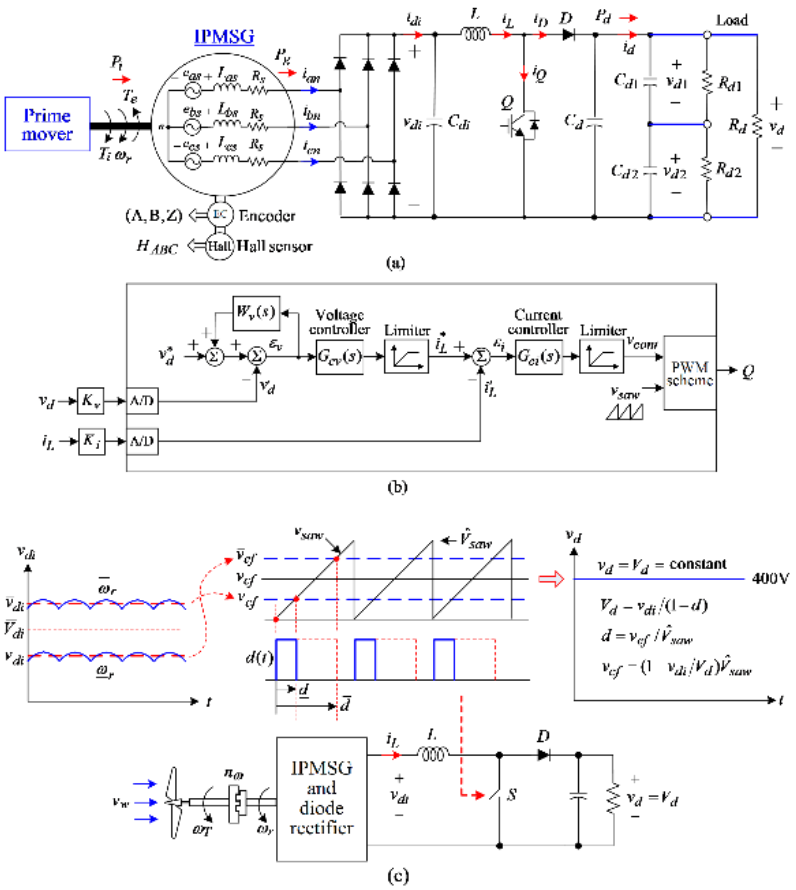

Figure 3 Wind IPMSG based bipolar DC microgrid with 3P1SW CCM boost SMR: (a) schematic; (b) control scheme; (c) The voltage transfer relationship under varied driving speed.

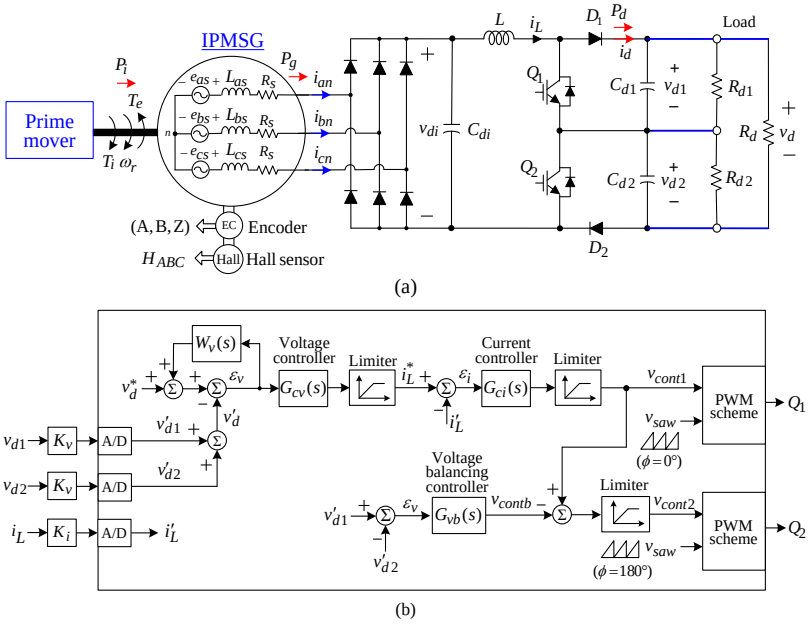

Figure 4 Wind IPMSG based bipolar DC microgrid with 3P2SW CCM boost SMR: (a) schematic; (b) control scheme.

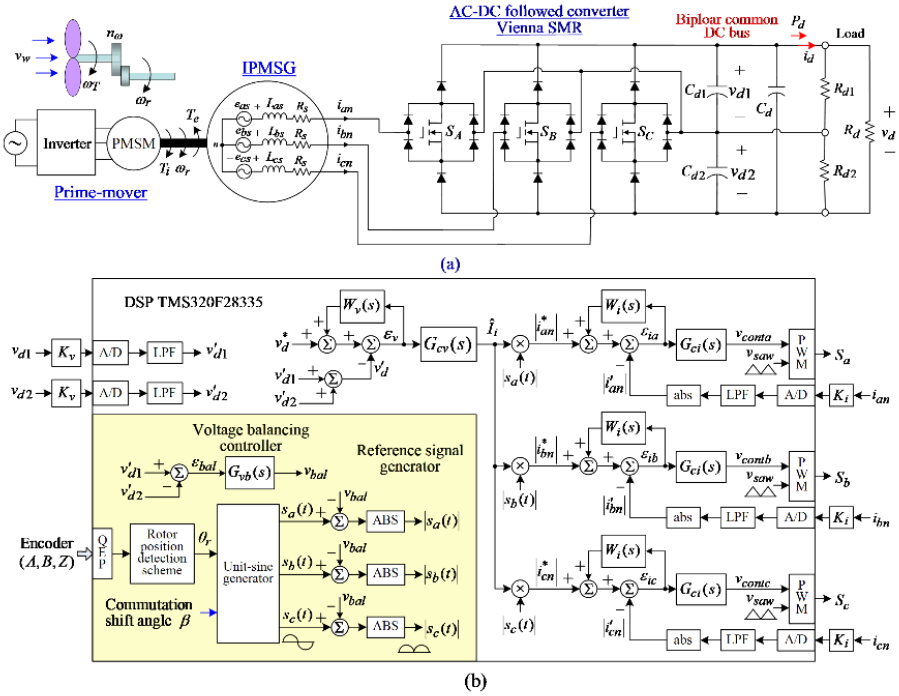

Figure 5 Wind IPMSG based bipolar DC microgrid with 3P3SW Vienna boost SMR: (a) schematic; (b) control scheme.

2.2 The Employed Machines

2.2.1 Governing Equations

The electromagnetic developed torque or retarding torque T_e of a PMSG in the *dq*-domain can be written as:

$$T_e = \frac{3}{2}\frac{P}{2}\left(\lambda'_m i^r_{qs} - \left(L_d - L_q\right)i^r_{ds} i^r_{qs}\right) = T_I - B\omega_r - J\frac{d\omega_r}{dt} \tag{1}$$

where P = pole numbers, B = total damping coefficient, J = total inertia constant, T_i = input torque. Let β be the phase angle between a-phase current phasor and the q-axis, i.e., $\tilde{I}_{as} = \sqrt{2}I_{as}\angle -\beta$, one can obtain the following expressions for the *d-q* current components and the developed torque:

$$\begin{bmatrix} i^r_{qs} \\ i^r_{ds} \end{bmatrix} = \begin{bmatrix} \sqrt{2}I_{as}\cos\beta \\ -\sqrt{2}I_{as}\sin\beta \end{bmatrix} \tag{2}$$

$$\sqrt{2}I_{as} = \sqrt{\left(i^r_{qs}\right)^2 + \left(i^r_{ds}\right)^2} \tag{3}$$

$$T_e = \frac{3}{2}\frac{P}{2}\left[\lambda'_m\sqrt{2}I_{as}\cos\beta + \left(L_d - L_q\right)I^2_{as}\sin 2\beta\right],\ L_d < L_q \tag{4}$$

Further, the electromagnetic developed power can be expressed as $P_e = T_e\omega_r$.

The first and second terms of equation (4) are known as magnet torque and reluctance torque, respectively. It should be noted that $L_d < L_q$ for an IPMSG, and the proper setting of β is required for maximizing T_e and P_e. For an SPMSG, only the magnet torque exists because of $L_d = L_q$, and $\beta = \beta_{\max} = 0^\circ$ can be set for yielding maximum values of T_e and P_e. On the contrary, in a wind IPMSG, one can adjust the value of β to reduce power generation when there is a surplus of energy for issuing the power conditioning control.

2.2.2 Key Parameters of the Employed SPMSM and IPMSG

In the studied experimental wind IPMSG, as shown in Figure 1, an inverter-fed SPMSM drive is employed as an alternative to the wind turbine. The key specifications and parameters of the used SPMSM and IPMSG are listed in Table 1.

Table 1 Key specifications of the employed SPMSM and IPMSG.

Yeli Electric & Machinery Co.	Prime-mover (SPMSM)	Wind generator (IPMSG)
Models	YBL 13S-115L.Z	IP-S71–135
Pole	8	6
Rated power	2 kW	1 kW
Rated speed	3000 rpm	3000 rpm
Rated torque	6.5 N·m	3.23 N·m
Rated current	11A (rms)	4.8A (rms)
Winding resistance	0.431 Ω	0.735 Ω
Winding inductance	L_s = 1.057 mH	L_d = 3.705 mH L_q = 6.83 mH
Peak of flux linkage	λ'_m = 0.122 Wb	λ'_m = 0.1236 Wb
Phase back-EMF constant	K_e = 27.1 V_{rms}/krpm	K_e = 27.45 V_{rms}/krpm

3. Non-Sinusoidal SMR Based Bipolar DC Microgrid

3.1 Wind IPMSG with 3P1SW DCM Boost SMR

3.1.1 Power Devices

The switch *Q* and diode *D* in Figures 2(a) and 3(a) and the devices (Q_1, Q_2) and (D_1, D_2) provided in Figure 4(a) are obtained using off-the-shelf IGBT Module CM100DY-12H (100 Amperes, 600 Volts) made by Powerex Inc.

3.1.2 Feasibility of the Employed IPMSG

The operation under DCM for the SMR is depicted in Figure 2(a); the inherent power factor correction function is preserved without an extra current controller. The control scheme with only a voltage loop is shown in Figure 2(b). Although the control is simple, the limitation of inductance for DCM operation must be considered.

To allow the successful operation of the SMR, the energy storage inductances must be small enough to ensure the DCM operation for the overall load range of the selected switching frequency

f_s and a complete half AC cycle. According to Table 1, it is understood that the phase back-EMF peak E_m under 3000 rpm is 116.47 V, and the maximum inductance $L_{as,\max} = 6.83$ mH. For the given $V_d =$ 400 V ($D = (400 - 116.47 \times \sqrt{3})/400 = 0.4958$), $P_d =$ 1 kW, the maximum value of the phase current can be calculated as $i_{al,\max} =$ 11.45A. Thus the estimated switching frequency for preserving the boundary condition (Upper bound of DCM) can be derived as $f_s = (E_m D)/(L_{al}\, i_{al,\max}) = 738$ Hz . Hence the allowed f_s is unreasonably low compared to the fundamental frequency of the generated voltage by the employed IPMSG to build the 400 V DC bus. Thus, the 3P1SW DCM SMR is not suitable to be the follow-up converter of the employed IPMSG, which has a large embedded winding inductance.

3.2 Wind IPMSG with 3P1SW CCM Boost SMR

3.2.1 Power Circuit

Figures 3(a) and 3(b) show the schematic and control scheme of the established DSP-based 3P1SW CCM SMR. The varied DC voltage generated V_{di} is boosted using the boost converter under CCM to establish a well-regulated DC-bus voltage V_d. Based on the generating characteristics of the employed IPMSG, the operating range estimated is as follows:

- $\underline{\omega}_r \le \omega_r \le \bar{\omega}_r$: 1500 rpm $\le \omega_r \le$ 3000 rpm
- $\underline{E}_m \le E_m \le \bar{E}_m$: 58.23V $\le E_m \le$ 116.47V; thus, 71.323 V $\le E_{ab}$(rms) $\le$ 142.65 V
- $\underline{V}_{di} \le v_{di} \le \bar{V}_{di}$: 100.86 V $\le v_{di} \le$ 201.73 V
- $V_d =$ 400 V by the PWM control of boost converter in CCM.

where $v_{di} = \sqrt{3}E_m$ is assumed.

Energy Storage Inductor. Under the varied v_{di} (100.86V ~ 201.73V), the $v_{di} = \bar{V}_{di} =$ 201.73V is selected as the worst case for the design of the developed wind IPMSG DC/DC boost converter. The rated output is set as ($V_d =$ 400 V, $P_d =$ 1 kW), and the switching frequency is chosen to be $f_s =$ 30 kHz.

According to the input and output voltages, the duty ratio is determined to be $D = 0.4958$ in the continuous current mode (CCM). The measured inductance and ESR of the wound inductor at 30 kHz are $L =$ 1.751 mH and $r_L =$ 63 mΩ. Hence the actual inductor current ripple is given as:

$$\Delta i_L = \frac{V_{di}\, D}{f_s L} = \frac{201.7 \times 0.4958}{30000 \times 1.751 \times 10^{-3}} = 1.9 \text{ A} \tag{5}$$

DC-Link Filtering Capacitor. The DC-link filtering capacitor $C_d =$ 2200 μF/450 V is chosen to yield the output voltage ripple:

$$\Delta v_d = \frac{\Delta Q}{C_d} = \frac{I_d D T_s}{C_d} = \frac{V_d D T_s}{R_d C_d} = 0.02 \text{ V} \tag{6}$$

3.2.2 Control Scheme

By applying the state-space averaging technique, the equivalent control block of the current-loop is derived and shown in Figure 6(a), wherein $K_{PWM} = 1$ is the PWM transfer factor, the current sensing factor, and the plant dynamic model is:

$$K_i(s) = \frac{K_i}{1+\tau_i s} \approx K_i = \ 0.04 \text{ (V/A)}, \tau_i = \ 3.18 \times 10^{-3} \text{ s} \tag{7}$$

$$G_{pi}(s) \triangleq \left.\frac{\Delta i_L(s)}{\Delta D(s)}\right|_{\Delta v_{dc}=0} = \frac{(R_d C_d s + 2)V_d}{R_d C_d L s^2 + L s + (1-D)^2 R_d} \tag{8}$$

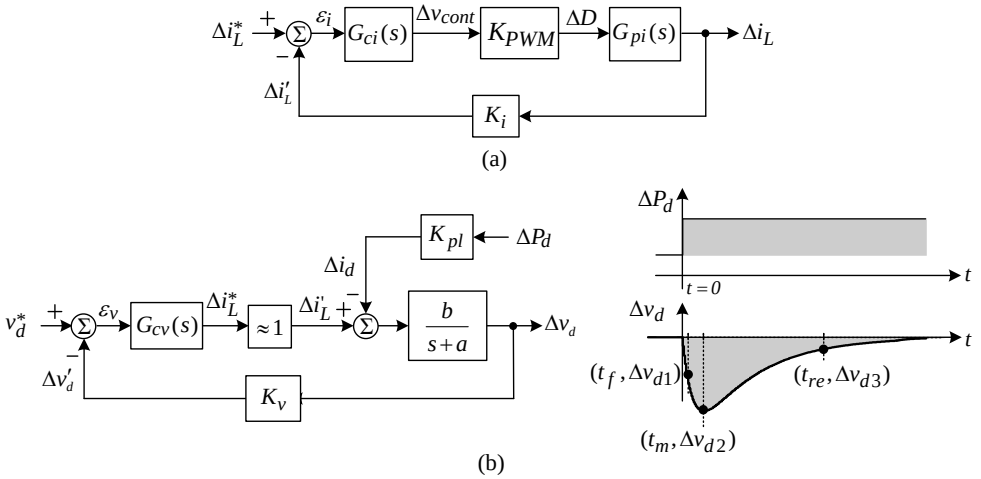

Figure 6 Dynamic models of DC/DC boost converter: (a) current-loop; (b) voltage-loop only with the feedback controller and the desired step load voltage regulation response.

Current Control Scheme. The current feedback controller is chosen to be the proportional-integral (PI) type having:

$$G_{ci}(s) = K_{pi} + \frac{K_{ii}}{s} \tag{9}$$

The design methodology lies in: (i) By applying the large-signal stability criterion, the upper limit of the P-gain is first determined to be $K_{pi} < 6.62$; And (ii) Choosing the I-gain $K_{ii} = 100$, the simulated Bode plots of the loop-gain for the current-loop shown in Figure 6(a) are used to determine the final P-gain $K_{pi} = \ 1.5$ with the crossover frequency of $f_c = \ 2.2$ kHz, accordingly:

$$G_{ci}(s) = \ 1.5 + \frac{100}{s} \tag{10}$$

Voltage Control Scheme.

(a) Voltage feedback controller

After having a well-designed current-loop, $\Delta i'_L = K_i(s)\Delta i_L \approx \Delta i_L^*$ can be reasonably assumed to yield the outer voltage-loop control block, as shown in Figure 6(b). The voltage sensing factor is given as:

$$K_v(s) = \frac{K_v}{1+\tau_v s} \approx K_v = \ 0.002 \text{ (V/V)}, \tau_v = \ 3.18 \times 10^{-3} \text{ s} \tag{11}$$

The voltage feedback controller, which is shown in Figure 6(b), is chosen to be the PI type, with:

$$G_{cv}(s) = K_{pv} + \frac{K_{iv}}{s} \tag{12}$$

The desired voltage response without overshooting due to the step load power change is also sketched in Figure 6(b). The design procedure is briefly described as follows:

(i) At the given operating point ($V_{di} =$ 183.84 V, $V_d =$ 400 V, $R_d =$ 300 Ω), the step-response approach is applied to yield the estimated plant model parameters:

$$K_{pl} = 1.35 \times 10^{-4}, a = 11.04, b = 1.2 \times 10^{4} \tag{13}$$

(ii) The voltage regulation response due to the step load power change of $\Delta P_d =$ 533 W ($R_d =$ 300 Ω → 150 Ω) is specified as $\Delta v_{dcm} = 10$ V and $t_{re} = 0.5$ s. With the known parameters (a, b, K_{pl}), the PI controller parameters can be derived to obtain ($K_{pv} = 2.688, K_{iv} = 15.17$). The measured results due to the same-step load change are shown in Figure 7. The correct voltage controller design process can be aware of from the results.

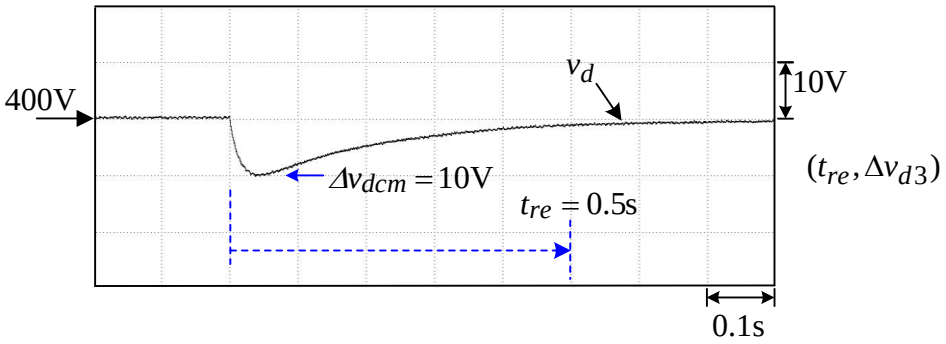

Figure 7 Measured voltage response by the designed voltage controller due to a step load change of $R_d =$ 300 Ω → 150 Ω ($\Delta P_d =$ 533 W).

(b) Robust controller

To enhance the control robustness, a simple, robust control scheme, as shown in Figure 3 is added. The robust weighting function is set as:

$$W_v(s) = \frac{W_v}{1 + \tau_v s} = \frac{W_v}{1 + 0.005s}, 0 \le W_v < 1 \tag{14}$$

It can be shown that: (i) The voltage tracking error ε_v yielded by PI control only can be reduced to $(1 - W_v)\,\varepsilon_v$ by adding the robust control; (ii) However, the controlled efforts would be magnified. Taking the compromised considerations, $W_v =$ 0.6 is chosen.

3.2.3 Experimental Results

The inverter-fed SPMSM driven IPMSG shown in Figure 3 is operated under the condition of ($V_{ab} =$ 142.65V/150Hz/3000rpm, $V_d =$ 400 V, $R_d =$ 150 Ω). The measured ($v_{an}, i_{an}, v_{di}, i_{di}, v_d$) are shown in Figure 8(a). Meanwhile, Figure 8(b) shows the measured steady-state i_L, (i_L^*, i_L') and (v_d^*, v_d') of the boost converter. Normal operation can be observed from the results. The DC bus voltage v_d' and the inductor current i_L' closely follow their commands.

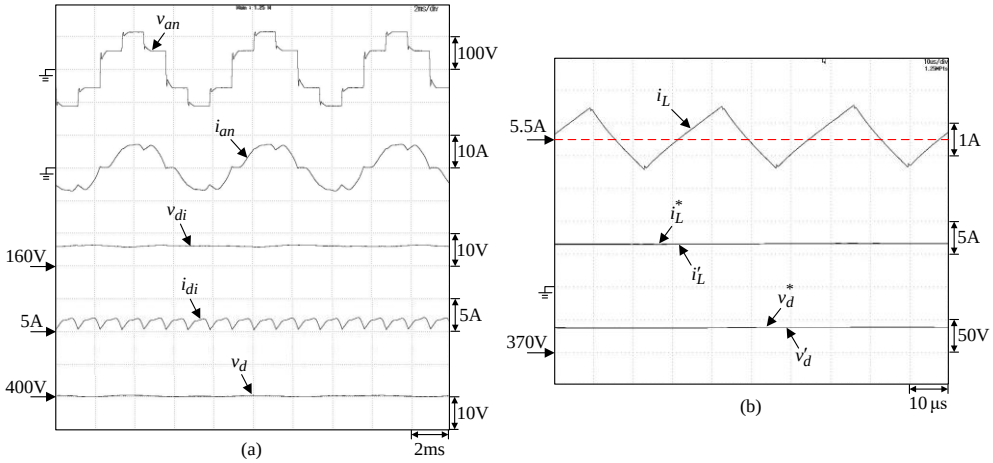

Figure 8 Measured results of the developed wind IPMSG with followed 3P1SW CCM SMR under ($V_{ab} = 142.65$V/150Hz/3000rpm, $v_d = 400$V, $R_d = 150\Omega$, $P_d = 1067$W) : (a) $(v_{an}, i_{an}, v_{di}, i_{di}, v_d)$; (b) $i_L, (i_L^*, i_L^{'})$ and (v_d^*, v_d') of the boost converter.

The measured v_d and i_L^* at ($V_d = 400$ V, $R_d = 300\,\Omega$) without ($W_v = 0$), and with robust control ($W_v = 0.6$) of the boost converter powered by the DC power supply at the DC-link with v_{di} due to a change in the step load of $R_d = 300\,\Omega \rightarrow 150\,\Omega$ are shown in Figure 9. The effectiveness of robust control in enhancing the regulation response can be understood from the results.

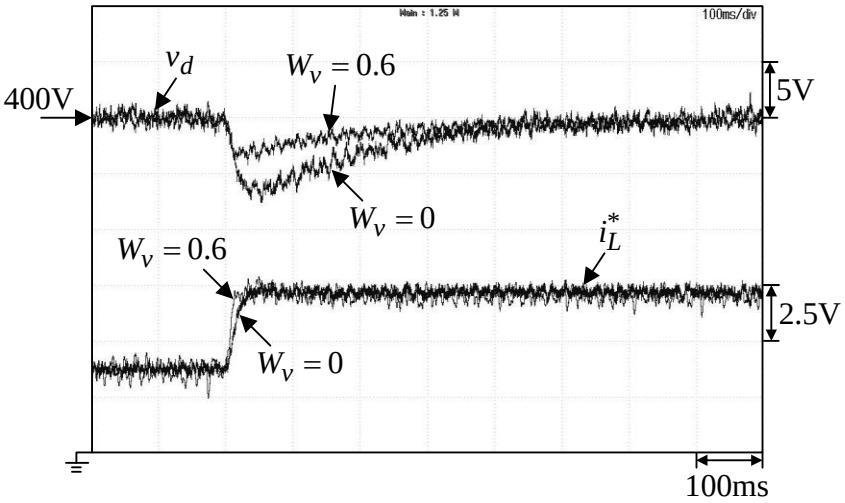

Figure 9 Measured v_d and i_L^* at ($V_{di} = 183.84$V, $V_d = 400$V, $R_d = 300\Omega$) without and with robust control due to a change in step load of $R_d = 300\,\Omega \rightarrow 150\,\Omega$.

Next, the robustness of generated voltage by the developed wind IPMSG against varying rotor speed is further assessed. The measured $\omega_r, v_{di}, v_d, i_L$and i_{an} at ($v_d = 400$V, $R_d = 150\,\Omega$) under varying rotor speeds of $\omega_r = 3000 \rightarrow 2500 \rightarrow 2000 \rightarrow 2500 \rightarrow 3000$ rpm are shown in Figure 10. Well regulated v_d under varying driven speed can be observed.

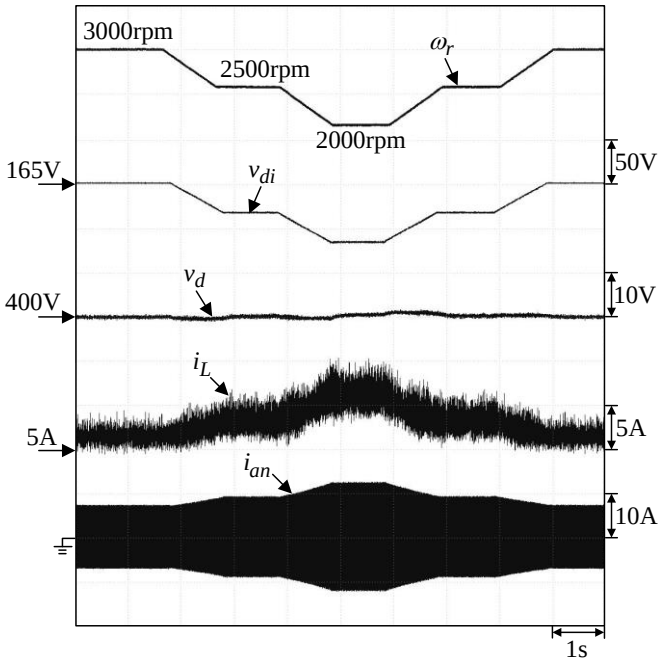

Figure 10 Measured $\omega_r, v_{di}, v_d, i_L$ and i_{an} of the developed wind IPMSG with followed 3P1SW CCM SMR at ($v_d = 400\,\text{V}, R_d = 150\,\Omega$) under varying rotor speed $\omega_r = 3000 \rightarrow 2500 \rightarrow 2000 \rightarrow 2500 \rightarrow 3000\text{rpm}$.

From the experimental results (not shown here), one can observe the imbalance between v_{d1} and v_{d2} as the bipolar DC-bus loads are not balanced. To improve this, one can add a voltage balancer across the DC-bus, or the following two SMRs are adopted.

3.2.4 Efficiency Assessment

To evaluate the efficiency of the established 3P1SW CCM SMR, the energy conversion efficiency assessment facility is arranged in Figure 11. Three power analyzers (using Yokogawa WT500 and HIOKI 3390 power analyzers) were used to measure the load power P_d and the two armature powers P_m and P_g of the SPMSM and the IPMSG, respectively.

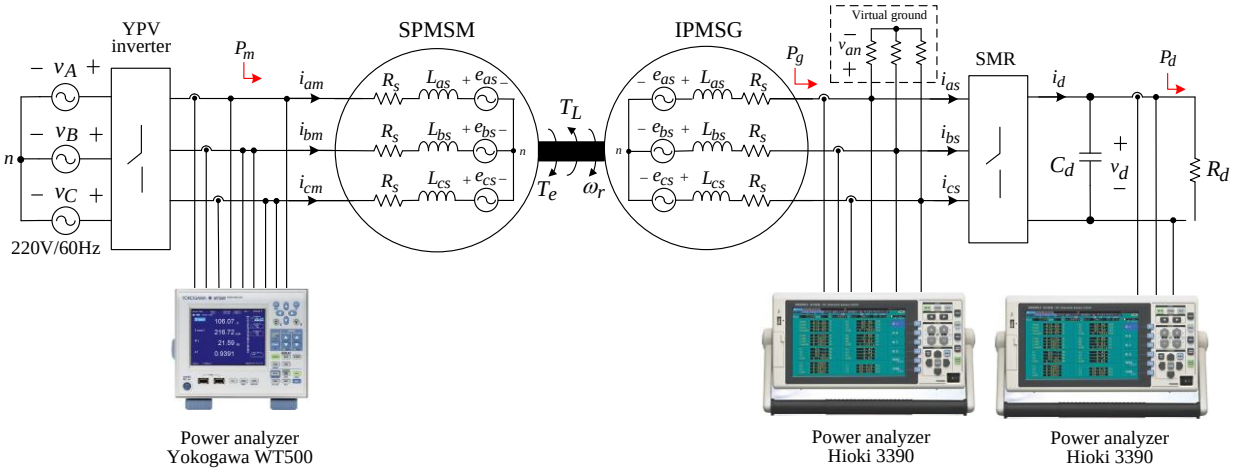

Figure 11 System configuration of efficiency measurement.

The output DC voltage $v_d = 400$ V is set, and the load resistance R_d is varied from 800 Ω to 160 Ω (P_d = 200 W to 1000 W). The related efficiencies were defined as $\eta_1 \triangleq P_g/P_m$, $\eta_2 \triangleq P_d/P_g$ (the efficiency of SMR), $\eta_3 \triangleq P_d/P_m = \eta_1\eta_2$, and $\eta_m \approx \eta_g \triangleq \sqrt{\eta_1}$. Since the machine shaft power cannot be measured directly, the IPMSG efficiency is approximately estimated from P_m and P_g by assuming $\eta_m \approx \eta_g$. The power-efficiency curves of η_g and η_2 are plotted in Figures 12(a) and 12(b).

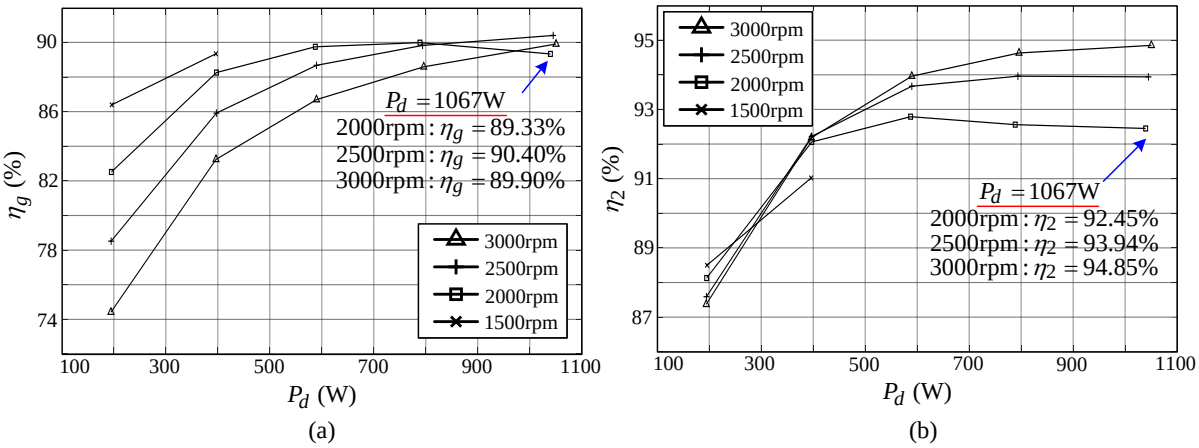

Figure 12 Efficiency curves of the developed wind IPMSG followed by 3P1SW CCM SMR under varied P_d and driven speed at $v_d = 400$ V: (a) η_g-P_d curve; (b) η_2-P_d curve.

3.3 Wind IPMSG with 3P2SW Three-Level CCM Boost SMR

3.3.1 Power Circuit

Figures 4(a) and 4(b) show the schematic and control scheme of the established 3P2SW CCM boost SMR. The ratings and switching frequency are identical to the 3P1SW CCM boost SMR provided in Sec. 3.2. The other key parameters are summarized below:

(1) Voltage transfer ratio: $V_d/V_{di} = 1/(1-D)$ in CCM.

(2) Energy storage inductor: $L = 684$ μH and ESR $r_L = 54$ mΩ at 30 kHz. The actual inductor current ripple can be calculated as $\Delta i_L = 41$ mA.

(3) DC-link filtering capacitors: $C_{d1} = C_{d2} = 2200$ μF

3.3.2 Control Scheme

Current Control Scheme. The current feedback controller is selected to be the proportional-integral (PI) type with:

$$G_{ci}(s) = K_{pi} + \frac{K_{ii}}{s} = 0.1 + \frac{50}{s} \tag{15}$$

Voltage Feedback Controller.

$$G_{cv}(s) = K_{pv} + \frac{K_{iv}}{s} = 4 + \frac{22}{s} \tag{16}$$

Robust Controller: Same as (14).

Voltage Balancing Control Scheme. From Figure 4(a) one can observe that the charging periods of C_{d1} and C_{d2} depends upon their PWM control voltages. Hence as shown in Figure 4(b), the voltage balancing of v_{d1} and v_{d2} can be achieved by modifying the control voltage for Q_2 as $v_{cont2} = v_{cont1} + v_{contb}$, along with v_{contb} being generated from a PI voltage balancing controller $G_{vb}(s)$. The parameters of $G_{vb}(s)$ are determined via the method of trial-and-error are as follows:

$$G_{vb}(s) = K_{pb} + \frac{K_{ib}}{s} = 5 + \frac{50}{s} \tag{17}$$

To observe the balanced voltage characteristics of the established bipolar DC-bus, let $R_{d1} = 75\,\Omega$ and R_{d2} be changed in the step between 75 Ω and 100 Ω. Figure 13(a) shows the measured $i_L, v_d, (v_{d1}, v_{d2})$ of the 3P2SW CCM SMR due to the step resistance change of $R_{d2} = 75\,\Omega \rightarrow 100\,\Omega \rightarrow 75\,\Omega$ at $(R_{d1} = 75\,\Omega, R_{d2} = 75\,\Omega)$ without the voltage balancer, and Figure 13(b) shows the measured $i_L, v_d, (v_{d1}, v_{d2})$ of the 3P2SW CCM SMR with voltage balancer. One could note the correctness of the voltage balancer.

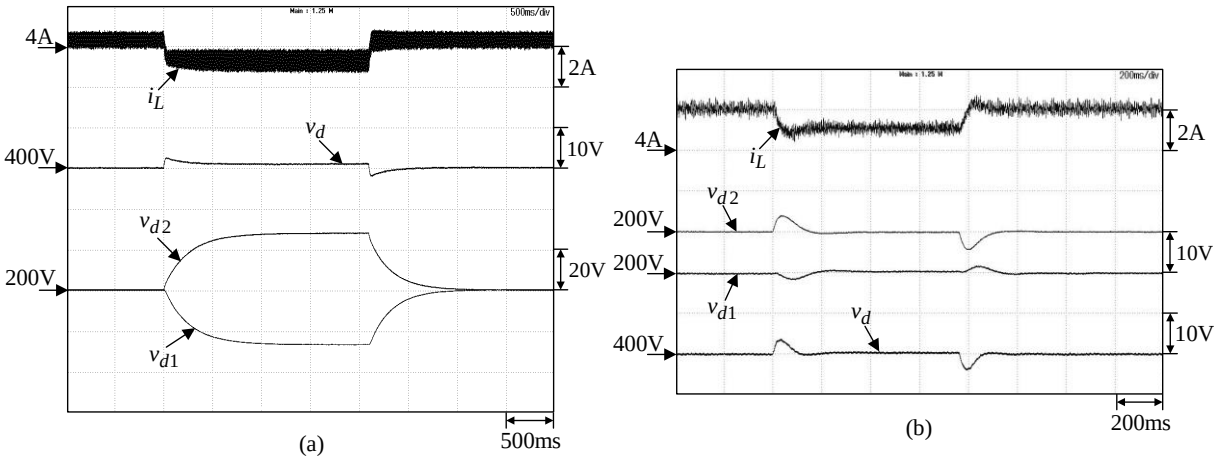

Figure 13 Measured $i_L, v_d, (v_{d1}, v_{d2})$ of the developed 3P2SW three-level DC/DC boost converter powered by the wind IPMSG at (3000 rpm, $v_d = 400\,\text{V}, R_{d1} = 75\,\Omega$, $R_{d2} = 75\,\Omega$) due to a step resistance change of $R_{d2} = 75\,\Omega \rightarrow 100\,\Omega \rightarrow 75\,\Omega$: (a) without voltage balancer; (b) with voltage balancer.

3.3.3 Experimental Results

The wind IPSMG is driven at 3000 rpm, and the measured $(v_{an}, i_{an}, v_{di}, i_L, v_d)$ of the developed Wind IPMSG along with the followed 3P2SW three-level boost SMR are shown in Figure 14(a). And the measuredi_L, (i_L^*, i_L') and (v_d^*, v'_d) of the three-level boost converter are plotted in Figure 14(b).

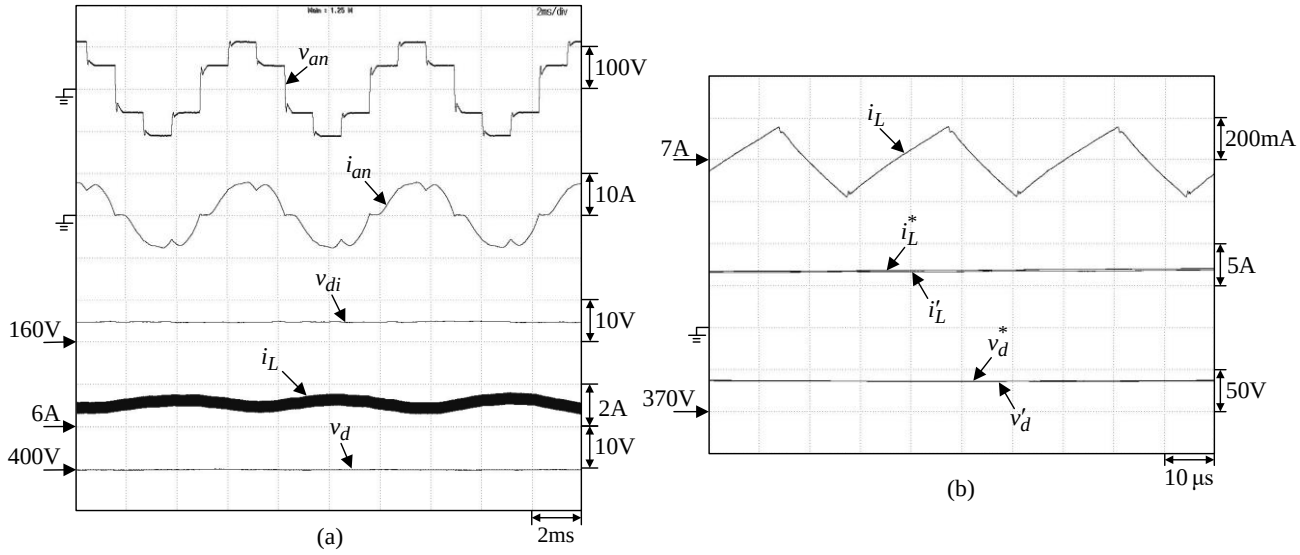

Figure 14 Measured results of the developed wind IPMSG along with the followed 3P2SW three-level boost SMR at 3000 rpm under $V_{ab} = 142.65$ V, $v_d = 400$ V and $R_d = 150\ \Omega, P_d = 1067$ W): (a) $(v_{an}, i_{an}, v_{di}, i_L, v_d)$; (b) i_L, (i_L^*, i'_L) and (v_d^*, v'_d) of the three-level boost converter.

The measured waveforms of $\omega_r, v_{di}, v_d, i_L$ and i_{an} at ($v_d = 400$ V, $R_d = 150\ \Omega$) of the wind IPMSG under varying rotor speed $\omega_r = 3000 \rightarrow 2500 \rightarrow 2000 \rightarrow 2500 \rightarrow 3000$ rpm are shown in Figure 15. Well regulated v_d can be observed under varying driven speeds.

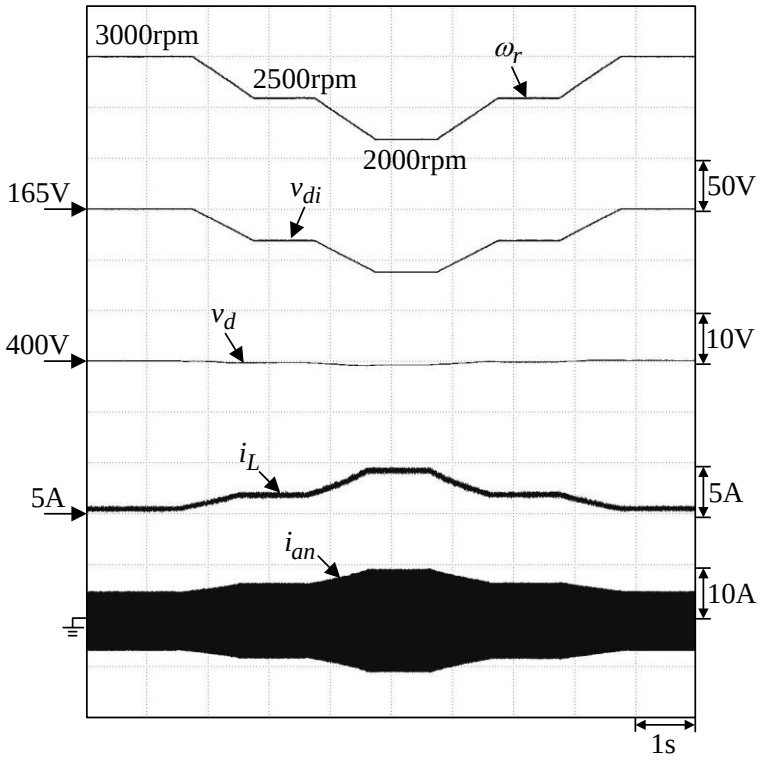

Figure 15 The measurement of $\omega_r, v_{di}, v_d, i_L$ and i_{an} of the developed wind IPMSG followed by 3P2SW three-level boost SMR at ($v_d = 400$V, $R_d = 150\ \Omega$) under varying rotor speed $\omega_r = 3000 \rightarrow 2500 \rightarrow 2000 \rightarrow 2500 \rightarrow 3000$ rpm.

3.3.4 Efficiency Assessment

The energy conversion efficiency measurement facility arranged in Figure 11 is also employed in this case. To measure the steady-state power characteristics, the output DC voltage v_d is set as a constant (400V). The load resistances R_{d1} and R_{d2} are set at five values from 400 Ω to 80 Ω ($P_d =$ 200W to 1000W). The power-efficiency curves of η_g and η_2 are plotted in Figures 16(a) and 16(b).

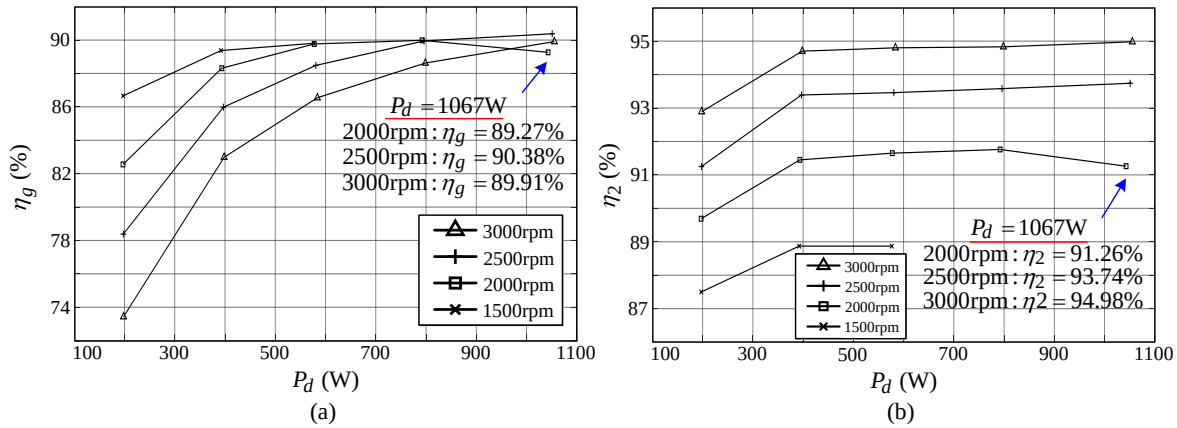

Figure 16 Efficiency curves of the developed wind IPMSG followed by 3P2SW three-level boost SMR under varied P_d and driven speed atv_d = 400 V: (a) η_g-P_d curve; (b) $\eta_2 - P_d$ curve.

4. Vienna SMR Based Bipolar DC Microgrid

To improve the limitations possessed by the non-sinusoidal SMRs presented in the previous section, the three-phase three-switch Vienna SMR could be adopted as the wind generator followed converter. The armature currents can be PWM controlled to have a sinusoidal waveform with a higher rating utilization. Meanwhile, the micro-grid bipolar DC bus is inherently established.

4.1 Power Circuit

Figures 5(a) and 5(b) show the schematic and control scheme of the established 3P3SW Vienna boost SMR. The designed key parameters are summarized below:

4.1.1 Energy Storage Inductor

Through careful derivation, one can express the phase current ripple as:

$$\Delta i_{an} = \left[\frac{6E_m V_d - 9E_m^2 + \left(3\sqrt{3}E_m - 2\sqrt{3}V_d\right)\omega_e L_{as} I_{an}}{6V_d}\right]\frac{T_s}{L_{as}} \tag{18}$$

The maximum current ripple occurs when $\omega_e t = \pi/2$. Normally, to operate in the CCM, the current ripple Δi_{an} is needed:

$$\Delta i_{an,\max} < 0.5 i_{an,\max} = 2.86 \text{ A} \tag{19}$$

where

$$i_{an.\max} = \frac{2}{3} \times \frac{P_d}{E_m} = \frac{2}{3} \times \frac{1000}{116.47} = 5.72 \text{ A} \tag{20}$$

The minimum inductance value $L_{as,\min}$ can be obtained as follows:

$$L_{as,\min} > \frac{\left(\sqrt{3}V_d - 1.5\sqrt{3}E_m\right)E_m}{\sqrt{3}\Delta i_{an,\max} V_d/T_s + \omega_e V_d I_{an} - 1.5\omega_e E_m I_{an}} = 764\ \mu\text{H} \tag{21}$$

From Table 1, the IPMSG winding inductance is much larger than $L_{as,\min}$

4.2 Control Scheme

4.2.1 Current Control Scheme

The current feedback controller is selected to be the proportional-integral (PI) type with:

$$G_{ci}(s) = K_{pi} + \frac{K_{ii}}{s} = 0.95 + \frac{500}{s} \tag{22}$$

To enhance the dynamic response of the DC-bus voltage regulation, the robust controller is also added with the weighting function:

$$W_i(s) = \frac{W_i}{1 + \tau_i s} = \frac{0.6}{1 + 0.005\text{s}} \tag{23}$$

4.2.2 Voltage Feedback Controller

$$G_{cv}(s) = K_{pv} + \frac{K_{iv}}{s} = 1.7 + \frac{8.8}{s} \tag{24}$$

4.2.3 Voltage Balancing Controller

In Figure 5(b), the voltage balancing controller is set as:

$$G_{vb}(s) = K_{pvb} + \frac{K_{ivb}}{s} = 5 + \frac{50}{s} \tag{25}$$

Figure 17(a) and Figure 17(b) show the measured $v_d, (v_{d1}, v_{d2})$ of the Vienna SMR due to a change in step resistance of $R_{d2} = 75\ \Omega \rightarrow 100\ \Omega$ at ($\omega_r = 3000$ rpm, $R_{d1} = 75\ \Omega$, $R_{d2} = 75\ \Omega$) without and with the voltage balancer. One can observe the correctness of the voltage balancing control.

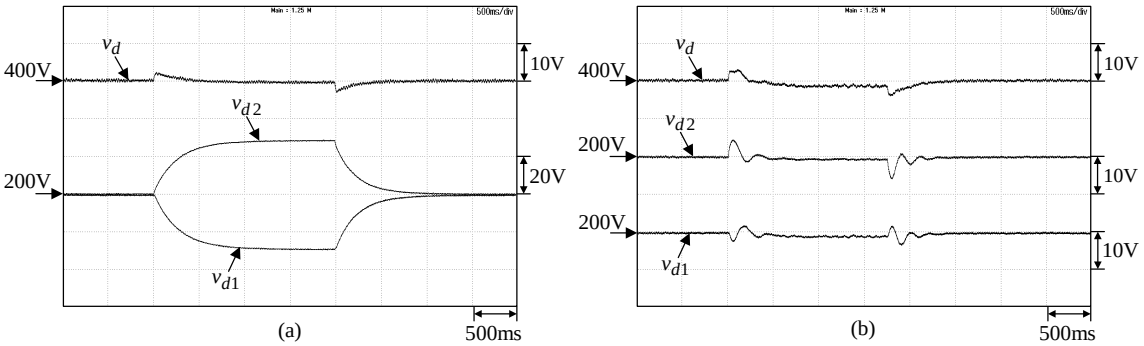

Figure 17 Measured $v_d, (v_{d1}, v_{d2})$ due to a step resistance change of $R_{d2} = 75\ \Omega \rightarrow 100\ \Omega \rightarrow 75\ \Omega$ at ($\omega_r = 3000$ rpm, $R_{d1} = 75\ \Omega$, $R_{d2} = 75\ \Omega$): (a) without voltage balancing control; (b) with voltage balancing control.

4.3 Experimental Results

4.3.1 Effects of the Commutation Angle Shift

For an IPMSG, the commutation shifting angle β can be included to improve the energy conversion efficiency. To observe the effectiveness of the shifting angle, the voltage loop of the Vienna SMR shown in Figure 5(b) is removed. By letting the output resistive loads be $R_d = 400\ \Omega$ and $200\ \Omega$ without R_{d1} and R_{d2}, the current command is manually tuned as $\hat{I}_i = 2$A and 3.98 A with $\beta = 0^\circ$ to result in the output voltage of 400 V. Starting from the initial point ($\beta = 0^\circ$), the shifting angle is set between –30° to 30° with $\Delta\beta = 2^\circ$. Figure 18 shows the relationships between the shifting angle β and the output voltage v_d. One can observe the influence of v_d and thus the $P_d = v_d^2/R_d$ by varying the β angle.

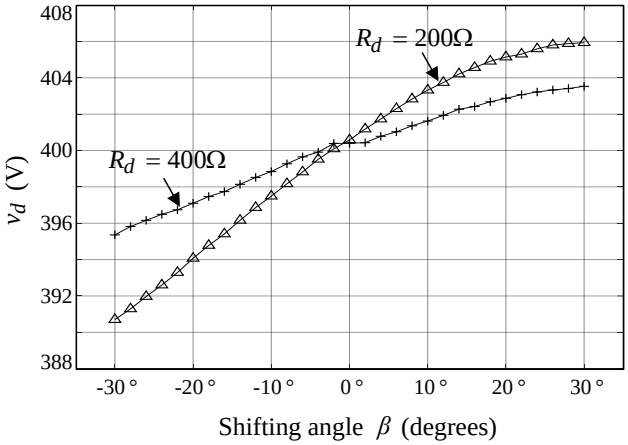

Figure 18 Relationships between the shifting angle β and v_d under two loads.

4.3.2 Operating Characteristics

The voltage loop is applied with $v_d^* = 400$ V. The steady-state characteristics of the IPMSG followed by the Vienna SMR with shifting angles $\beta = -30°$ and $\beta = +30°$ under two resistive loads are listed in Table 2. From Figure 18 and Table 2, one can understand the effects of commutation angle on the IPMSG generating characteristics.

Table 2 Measured steady-state characteristics of the IPMSG followed by Vienna SMR at 3000 rpm under two shifting angles β.

$v_d = 400$V, $R_d = 400\ \Omega$, $P_d = 400$W							
β	V_{an} (V)	I_{as} (A)	PF	V_d (V)	P_g (W)	P_d (W)	η (%)
-30°	79.71	1.79	0.97	399.43	422	392	92.79
30°	81.06	1.72	0.99	400.12	421	393	93.31
$v_d = 400$V, $R_d = 200\ \Omega$, $P_d = 800$W							
β	V_{an} (V)	I_{as} (A)	PF	V_d (V)	P_g (W)	P_d (W)	η (%)
-30°	77.7	3.64	0.97	399.41	834	783	93.84
30°	82.24	3.39	0.98	401.35	830	793	95.47

Let the wind IPMSG be driven at $\omega_r =$ 3000 rpm with a load of ($v_d =$ 400 V, $R_d = 150\ \Omega$). The measured $(i_{an}, i_{bn}, i_{cn}), i_{an}, v_{an}, v_d$ are shown in Figure 19. Compared to the i_{an} of Figure 19 to the ones depicted in Figures 8 and 14, one can find that the slightly better waveform is yielded by the Vienna SMR. Meanwhile, the measured waveforms of ω_r, v_d, i_{an} and v_{an} at ($v_d =$ 400 V, $R_d =$ 150 Ω) of the wind IPMSG system under the varying speed of $\omega_r = 3000 \rightarrow 2500 \rightarrow 2000 \rightarrow 2500 \rightarrow 3000$ rpm are shown in Figure 20. The well regulated v_d under varying driven speed can be observed.

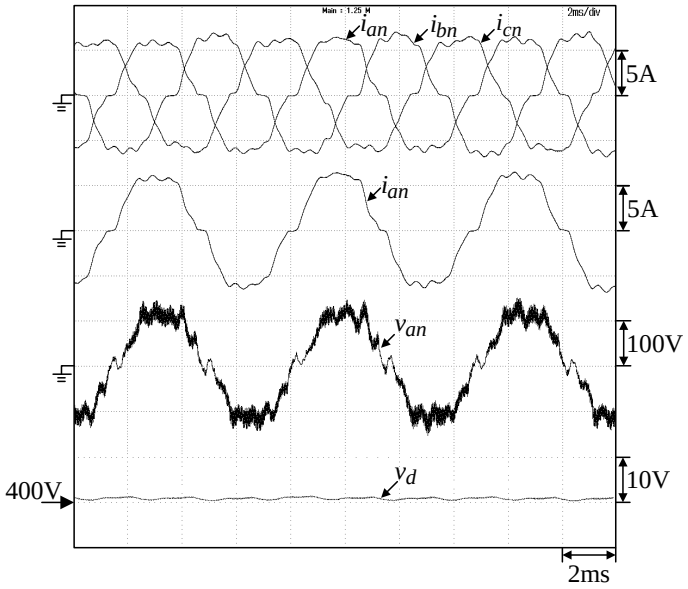

Figure 19 Measured (i_{an}, i_{bn}, i_{cn}), i_{an}, v_{an}, v_d of the wind IPMSG with Vienna SMR followed by at ($\omega_r =$ 3000 rpm, $v_d =$ 400 V, $R_d = 150\ \Omega$).

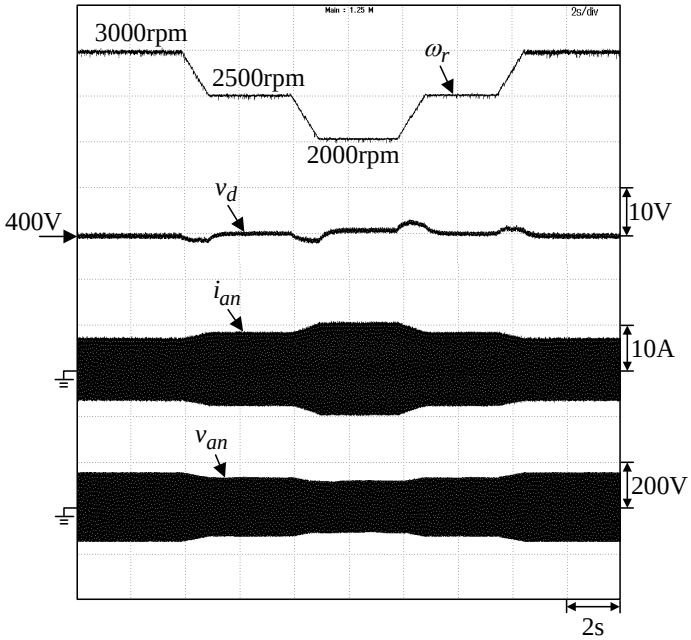

Figure 20 Measured ω_r, v_d, i_{an} and v_{an} of the wind IPMSG along with the following Vienna boost SMR at ($v_d =$ 400 V, $R_d = 150\ \Omega$) under varying rotor speed $\omega_r = 3000 \rightarrow 2500 \rightarrow 2000 \rightarrow 2500 \rightarrow 3000$ rpm.

To measure the steady-state power characteristics, the output DC voltage v_d is set as a constant (400 V). The load resistances R_{d1} and R_{d2} are set according to five values from 400 Ω to 80 Ω ($P_d =$ 200 W to 1000 W). The power-efficiency curves of η_g and η_2 (Efficiency of the SMR) are plotted in Figures 21(a) and 21(b). While comparing the results plotted in Figure 21 to those shown in Figures 12 and 16, one can observe the slightly higher η_g and η_2 by applying the Vienna SMR as the wind generator followed converter.

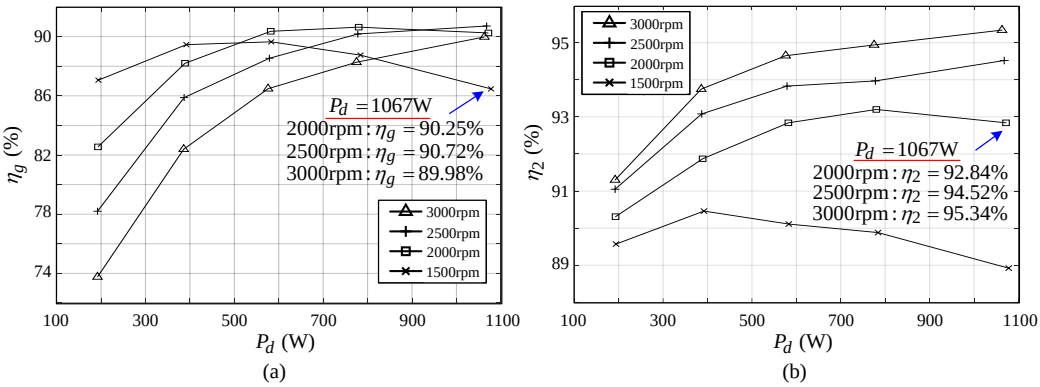

Figure 21 Efficiency curves of the developed wind IPMSG followed by 3P3SW Vienna boost SMR under varied P_d and driven speed at $v_d =$ 400 V: (a) $\eta_g - P_d$ curve; (b) $\eta_2 - P_d$ curve.

5. Conclusions

This paper has presented the development of wind interior IPMSG based bipolar DC microgrids consisting of various switch-mode rectifiers. Some interpretation can be concluded from the experimental explorations: (i) Through the proposed robust voltage and current controls, a well-regulated microgrid DC-bus voltage is established; (ii) 3P1SW DCM and CCM boost SMRs having a passive capacitor leg to form bipolar DC-bus do not have voltage balancing capabilities. To improve this, an extra voltage balancer leg must be added; (iii) Normally, the 3P1SW DCM SMR is not suitable to be the followed converter of the IPMSG having a large embedded winding inductance; (iv) Both, the 3P2SW three-level boost SMR and the 3P3SW Vienna SMR can naturally form the bipolar DC-bus, and the voltage balancing can be preserved via proper control. Compared to the former, the Vienna SMR has a slightly better power quality on the AC side and efficiencies of the SMR schematic.

Author Contributions

Xiang-Yu Sun: Main author involving the measurements and the paper writing; Ping-Hong Jhou: Assisting the author and doing the proofreading; Min-Ze Lu: Assisting the author and doing the proofreading; Chang-Ming Liaw: Advisor giving suggesting and doing the proofreading.

Competing Interests

The authors have declared that no competing interests exist.

References

1. Che L, Shahidehpour M, Alabdulwahab A, Al-Turki Y. Hierarchical coordination of a community microgrid with AC and DC microgrids. IEEE Trans Smart Grid. 2015; 6: 3042-3051.
2. Kakigano H, Miura Y, Ise T. Low-voltage bipolar-type DC microgrid for super high quality distribution. IEEE Trans Power Electron. 2010; 25: 3066-3075.
3. Hu KW, Liaw CM. Incorporated operation control of DC microgrid and electric vehicle. IEEE Trans Ind Electron. 2016; 63: 202-215.
4. Dragičević T, Lu XN, Vasquez JC, Guerrero JM. DC microgrids- part I: A review of control strategies and stabilization techniques. IEEE Trans Power Electron. 2016; 31: 4876-4891.
5. Dragičević T, Lu XN, Vasquez JC, Guerrero JM. DC microgrids- part II: A review of power architectures, applications, and standardization issues. IEEE Trans Power Electron. 2016; 31: 3528-3549.
6. Krause PC, Wasynczuk O, Sudhoff SD. Analysis of electric machine and drive system. 2nd ed. Hoboken, New Jersey: Wiley; 2002.
7. Zeraoulia M, Benbouzid ME, Diallo D. Electric motor drive selection issues for HEV propulsion systems: A comparative study. IEEE Trans Veh Technol. 2006; 55: 1756-1764.
8. Pellegrino G, Vagati A, Boazzo B, Guglielmi P. Comparison of induction and PM synchronous motor drives for EV application including design examples. IEEE Trans Ind Appl. 2012; 48: 2322-2332.
9. Yang Z, Shang F, Brown IP, Krishnamurthy M. Comparative study of interior permanent magnet, induction, and switched reluctance motor drives for EV and HEV applications. IEEE Trans Transp Electrific. 2015; 1: 245-254.
10. Menon R, Kadam AH, Azeez NA, Williamson SS. A comprehensive survey on permanent magnet synchronous motor drive systems for electric transportation applications. Proceedings of the IECON 2016 - 42nd Annual Conference of the IEEE Industrial Electronics Society; 2016 October 23-26; Florence, Italy. Manhattan, New York: IEEE.
11. Yaramasu V, Wu B, Sen PC, Kouro S, Narimani M. High-power wind energy conversion systems: State-of-art and emerging technologies. Proc IEEE. 2015; 103: 740-788.
12. Rajaei AH, Mohamadian M, Varjani AY. Vienna-rectifier-based direct torque control of PMSG for wind energy application. IEEE Trans on Ind Electron. 2013; 60: 2919-2929.
13. Hu KW, Liaw CM. A position sensorless surface-mounted permanent- magnet synchronous generator and its operation control. IET Power Electron. 2015; 8: 1636-1650.
14. Singh B, Singh BN, Chandra A, Al-Haddad K, Pandey A, Kothari DP. A review of three-phase improved power quality AC-DC converter. IEEE Trans Ind Electron. 2004; 51: 641-660.
15. Friedli T, Kolar JW. The essence of three-phase PFC rectifier systems- Part I. IEEE Trans Power Electron. 2013; 28: 176-198.
16. Friedli T, Hartmann M, Kolar JW. The essence of three-phase PFC rectifier systems- Part II. IEEE Trans Power Electron. 2014; 29: 543-560.
17. Chai JY, Chang YC, Liaw CM. On the switched-reluctance motor drive with three-phase single-switch switch-mode rectifier front-end. IEEE Trans Power Electron. 2010; 25: 1135-1148.
18. Zhang Y, Shi JL, Zhou L, Li J, Sumner M, Wang P, et al. Wide input-voltage range boost three-level DC–DC converter with quasi-Z source for fuel cell vehicles. IEEE Trans Power Electron. 2017; 32: 6728-6738.

19. Kolar JW, Drofenik U, Zach FC. Current handling capability of the neutral point of a three-phase/switch/level boost-type PWM (VIENNA) rectifier. Proceedings of the 27th Annual IEEE Power Electronics Specialists Conference; 1996 June 23-27; Baveno, Italy. Manhattan, New York: IEEE.
20. Hu KW, Liaw CM. Development of a wind interior permanent-magnet synchronous generator based microgrid and its operation control. IEEE Trans Power Electron. 2015; 30: 4973-4985.
21. Mohan N, Undeland TM, Robbins WP. Power electronics converters, applications and design. 3rd ed. New Jersey: John Wiley & Sons; 2003.
22. Tan NM, Abe T, Akagi H. Design and performance of a bidirectional isolated DC-DC converter for a battery energy storage system. IEEE Trans Power Electron. 2012; 27: 1237-1248.
23. Cornea O, Guran E, Muntean N, Hulea D. Bi-directional hybrid DC-DC converter with large conversion ratio for microgrid DC busses interface. Proceedings of the 2014 International Symposium on Power Electronics, Electrical Drives, Automation and Motion; 2014 June 18-20; Ischia, Italy. Manhattan, New York: IEEE.
24. Kondrath N. Bidirectional DC-DC converter topologies and control strategies for interfacing energy storage systems in microgrids: An overview. Proceedings of the 2017 IEEE International Conference on Smart Energy Grid Engineering (SEGE); 2017 August 14-17; Oshawa, ON, Canada.
25. Forouzesh M, Siwakoti YP, Gorji SA, Blaabjerg F, Lehman B. Step-up DC/DC converters: A comprehensive review of voltage-boosting techniques, topologies, and applications. IEEE Trans Power Electron. 2017; 32: 9143-9178.
26. Dahalea S, Dasb A, Pindoriya NM, Rajendran S. An overview of DC-DC converter topologies and controls in DC microgrid. Proceedings of the 7th International Conference on Power Systems (ICPS); 2017 December 21-23; Pune, India.
27. Kan ZZ, Li PC, Yuan RR, Zhang CJ. Interleaved three-level bi-directional DC-DC converter and power flow control. Proceedings of the 3rd International Conference on Intelligent Green Building and Smart Grid (IGBSG); 2018 April 22-25; Yilan, Taiwan.
28. Zhang XN, Wang BF, Manandhar U, Gooi HB, Foo G. A model predictive current controlled bidirectional three-level DC/DC converter for hybrid energy storage system in DC microgrids. IEEE Trans Power Electron. 2019; 34: 4025–4030.
29. Bhaskar MS, Ramachandaramurthy VK, Padmanaban S, Blaabjerg F, Ionel DM, Mitolo M, et al. Survey of DC-DC non-isolated topologies for unidirectional power flow in fuel cell vehicles. IEEE Access. 2020; 8: 178130-178166.
30. Chiang SJ, Liaw CM. A single-phase three-wire transformerless inverter. IET Proc Electr Power Appl. 1994; 141: 197-205.
31. Hava AM, Kerkman RJ, Lipo TA. Simple analytical and graphical methods for carrier-based PWM-VSI drives. IEEE Trans Power Electron. 1999; 14: 49-61.
32. Castilla M, Miret J, Matas J, de Vicuña LG, Guerrero JM. Control design guidelines for single-phase grid-connected photovoltaic inverters with damped resonant harmonic compensators. IEEE Trans Ind Electron. 2009; 56: 4492-4501.
33. Wue YS, Chang LC, Kjær SB, Bordonau J, Shimizu T. Topologies of single-phase inverters for small distributed power generators: An overview. IEEE Trans Power Electron. 2004; 19: 1305-1314.
34. Hu KW, Liaw CM. On an auxiliary power unit with emergency AC power output and its robust controls. IEEE Trans Ind Electron. 2013; 60: 4387-4402.

Enjoy *JEPT* by:

1. Submitting a manuscript
2. Joining in volunteer reviewer bank
3. Joining Editorial Board
4. Guest editing a special issue

For more details, please visit:
http://www.lidsen.com/journal/jept